minerals

MDPI

Article

Genesis of the Sanhetun Tellurium–Gold Deposit, Northeast China: Constraints from In Situ Elemental and Sulfur Isotopic Compositions of Pyrite

Mengmeng Zhang [1,2,3], Junfeng Shen [1,2], Chenglu Li [4,*], M. Santosh [1,5,6], Kexin Xu [7], Gexue Zhao [1] and Huajuan Gu [4]

1 School of Earth Sciences and Resources, China University of Geosciences, Beijing 100083, China; mmzhang0615@163.com (M.Z.); shenjf@cugb.edu.cn (J.S.); santosh@cugb.edu.cn (M.S.); zhaogx@email.cugb.edu.cn (G.Z.)
2 Research Center of Genetic Mineralogy, School of Earth Sciences and Resources, China University of Geosciences, Beijing 100083, China
3 School of Gemology, China University of Geosciences, Beijing 100083, China
4 Natural Resources Survey Institute of Heilongjiang Province, Harbin 150036, China; guhuajuan02@163.com
5 Department of Earth Science, University of Adelaide, Adelaide, SA 5005, Australia
6 Curtin Malaysia Research Institute, Curtin University, CDT 250, Miri 98009, Malaysia
7 School of Earth Sciences and Engineering, Nanjing University, Nanjing 210023, China; xukexin@nju.edu.cn
* Correspondence: lcl230881@163.com

Abstract: The Sanhetun tellurium–gold (Te–Au) deposit, located in the Duobaoshan polymetallic metallogenic belt (DPMB) within the eastern section of the Central Asian Orogenic Belt (CAOB), is a newly discovered small-scale gold deposit. The mineralization, with a resource of ≥4 t Au, is mainly hosted in three NNE-trending alteration zones between Early Carboniferous granitic mylonite and Lower Cretaceous volcanogenic-sedimentary formations. The genesis of formation of this deposit is poorly constrained. Here, we report the results of petrographic studies, TESCAN Integrated Mineral Analyzer (TIMA), major and trace element concentrations, and in situ S isotopes of pyrite. The results show that there are four types of pyrite: coarse-grained euhedral Py1, fine-grained quartz-Py2 vein crosscutting Py1, anhedral aggregated Py3, and anhedral aggregated Py4. The pre-ore stage Py1 contains negligible Au, Te, and other trace elements and has a relatively narrow range of $\delta^{34}S$ values ranging from −1.20 to −0.57‰. Py2 has higher concentrations of Au and Te and distinctly high concentrations of Mo, Sb, Zn, and Mn with markedly positive $\delta^{34}S$ values of 4.67 to 14.43‰. The main-ore stage Py3 contains high Au and Te concentrations and shows narrow $\delta^{34}S$ values ranging from −5.69 to 0.19‰. The post-ore stage Py4 displays low Au concentrations with the $\delta^{34}S$ values ranging from 2.66 to 3.86‰. Tellurides are widespread in Py3 and Py4, consisting mainly of native tellurium, tetradymite, tsumoite, hessite, and petzite. Especially, tetradymite commonly coexists with native gold. This study highlights the role of Te–Bi–S melt as an important gold scavenger in As-deficient ore-forming fluids.

Keywords: telluride; pyrite; sulfur isotope; Sanhetun tellurium–gold deposit

Citation: Zhang, M.; Shen, J.; Li, C.; Santosh, M.; Xu, K.; Zhao, G.; Gu, H. Genesis of the Sanhetun Tellurium–Gold Deposit, Northeast China: Constraints from In Situ Elemental and Sulfur Isotopic Compositions of Pyrite. *Minerals* **2024**, *14*, 1014. https://doi.org/10.3390/min14101014

Academic Editor: Paul Alexandre

Received: 7 August 2024
Revised: 2 October 2024
Accepted: 3 October 2024
Published: 8 October 2024

1. Introduction

The Duobaoshan polymetallic metallogenic belt (DPMB) is an important Au–Cu–Mo–Fe ore field in NE China with numerous ore deposits, including the Zhengguang epithermal Au-Zn deposit, the Tongshan and Duobaoshan porphyry Cu–Mo deposits, and the Sankuanggou and Xiaoduobaoshan Fe skarn deposits [1–5]. In this belt, there is a large-scale NE-trending granitic mylonite ductile shear zone with a maximum width of 25 km, within which a series of gold deposits were discovered, including the Sandaowanzi [6], Yongxin [7–9], Mengdehe [10], and Beidagou [11] deposits. Notably, these deposits show significant tellurium enrichment, which is testified by the occurrence of telluride phases. The

telluride commonly shows a close relationship with Au mineralization, especially in the Sandaowanzi gold deposit, which is a telluride-dominant epithermal gold deposit. Previous studies focused on the Au mineralization with not much attention paid to the Te enrichment mechanism and Te–Au relationship. In recent years, tellurium has been listed as a critical metal [12] due to its potential application in the fields of photovoltaic cell, semiconductor materials, and laser ladar [13–15], thus adding important significance to such types of deposits.

The Sanhetun Te–Au deposit, located in the southwestern part of the DPMB, is a newly discovered small-scale gold deposit in the extreme southwestern part of the ductile shear zone. A number of tellurides were also recognized in this deposit [16]. However, the mineralogical and minero-chemical occurrence state, source, and relationship with Au remain poorly understood. In this contribution, we present the results from telluride mineralogy, in situ trace element compositions, and sulfur isotope compositions of multiple types of pyrite. The main objective is to investigate the occurrence state of Te, enrichment mechanism of Au, as well as genesis of multiple types of pyrite from the Sanhetun Te–Au deposit.

2. Geological Settting

2.1. Reginal Geology

The Duobaoshan polymetallic metallogenic belt (DPMB) is an important Cu–Au–Mo–Fe ore field in NE China and is located in the suture zone of the Xing'an and Songnen blocks within the eastern part of the Central Asian Orogenic Belt (CAOB) (Figure 1a). The CAOB has been documented as the largest Phanerozoic accretionary orogen and the most-researched orogenic belt in the world [17]. The Sanhetun Te–Au deposit occurs at the southwestern part of the DPMB (Figure 1b).

The regional units are dominantly composed of the Neoarchean Xinkailing Formation, the Neoproterozoic to Lower Cambrian Galashan Formation, and the Beikuanhe Formation, primarily composed of schist, gneiss, amphibolite, and felsic volcanic rocks. The Ordovician units from old to young are as follows: the Tongshan Formation consists of a sequence of sandstone interbedded with dolomite; the Duobaoshan Formation is composed of andesite, dacite, and volcanogenic-sedimentary rocks; the Luohe Formation and Aihui Formation consist of interlayered metamorphosed sandstone, tuffaceous sandstone, and shale; the Silurian Huanghuagou Formation is a sequence of sandstone and siltstone. The Devonian Niqiuhe Formation consists of tuffaceous sandstone with interbeds of volcanic rocks. The Carboniferous-Permian Baoligaomiao Formation is mainly composed of intermediate-felsic volcanic rocks and volcaniclastic rocks. The Cretaceous units consist of the Longjiang Formation, Guanghua Formation, Jiufengshan Formation, and Ganhe Formation, primarily composed of a suite of intermediate-mafic to intermediate-felsic volcanic rocks, volcaniclastic rocks, and volcanogenic-sedimentary rocks. The Cenozoic units are mainly represented by the Daxiongshan basalt. The intrusive rocks include early to middle Ordovician diorite, granodiorite and granodiorite porphyry, Early Carboniferous to Late Permian diorite granite, syenite, diorite, monzonite, and alkali feldspar granite. Late Triassic to early to middle Jurassic magmatic rocks are composed of ultramafic rocks, gabbro, diorite granite, granodiorite, and quartz diorite. The Cretaceous magmatic rocks are mainly granite, granite porphyry, as well as vein rocks. The regional structure shows northeast and northwest trends, with secondary faults trending in east–west and north–south directions. The northwest-trending faults formed earlier, controlling the distribution of early Paleozoic units and Cu (Mo), Au, and Ag deposits. The northeast-trending faults formed slightly later, controlling the distribution of regional late Paleozoic granites, Mesozoic volcanic rocks, and Au deposits [18,19].

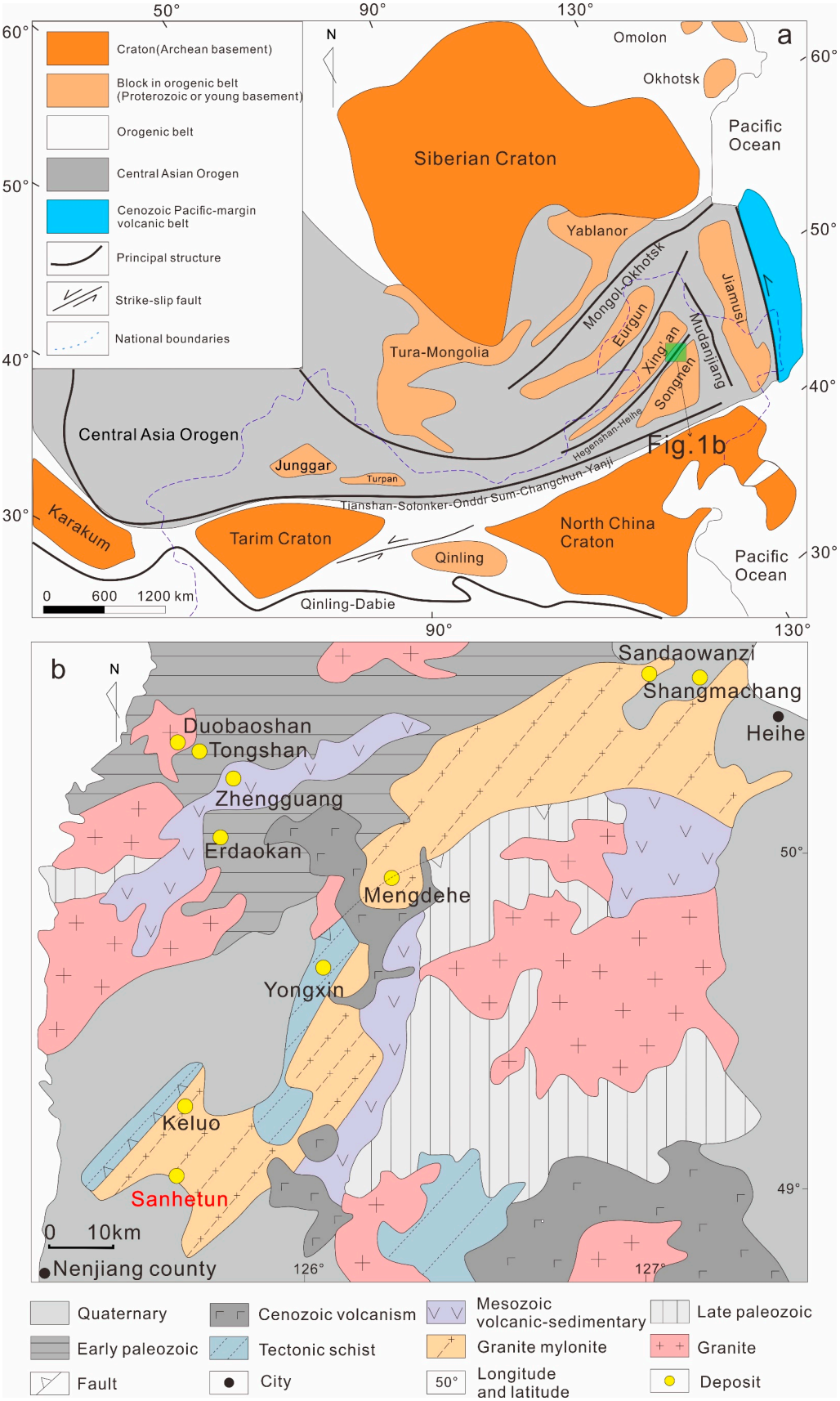

Figure 1. The geology of the study area: (**a**) schematic tectonic map of the Central Asia Orogenic Belt (modified after [20]); (**b**) geological map of the Duobaoshan polymetallic metallogenic belt (modified after [21]).

2.2. Deposit Geology

The ore bodies are primarily located at the structural interfaces between the Lower Cretaceous Jiufengshan Formation and Ganhe Formation, which are composed of volcanogenic-sedimentary rock assemblages, and the Early Carboniferous granitic mylonite (Figure 2). The exposed units in the mining area are mainly of Mesozoic volcanogenic-sedimentary rocks: the Guanghua Formation of the Lower Cretaceous is composed of intermediate to felsic volcanic sedimentary rocks, the Jiufengshan Formation consists of fine clastic sedimentary rocks interbedded with intermediate volcanic rocks, and the Ganhe Formation comprises intermediate-mafic volcanic rocks. The Upper Cretaceous Nenjiang Formation, consisting of mudstone and shale, unconformably overlies the aforementioned stratigraphic units. The intrusive rocks are mainly Early Carboniferous monzogranite and granodiorite, locally subjected to dynamic metamorphism forming mylonite and ultramylonite. The granitic mylonite is crosscut by diorite porphyrite dykes and quartz veins.

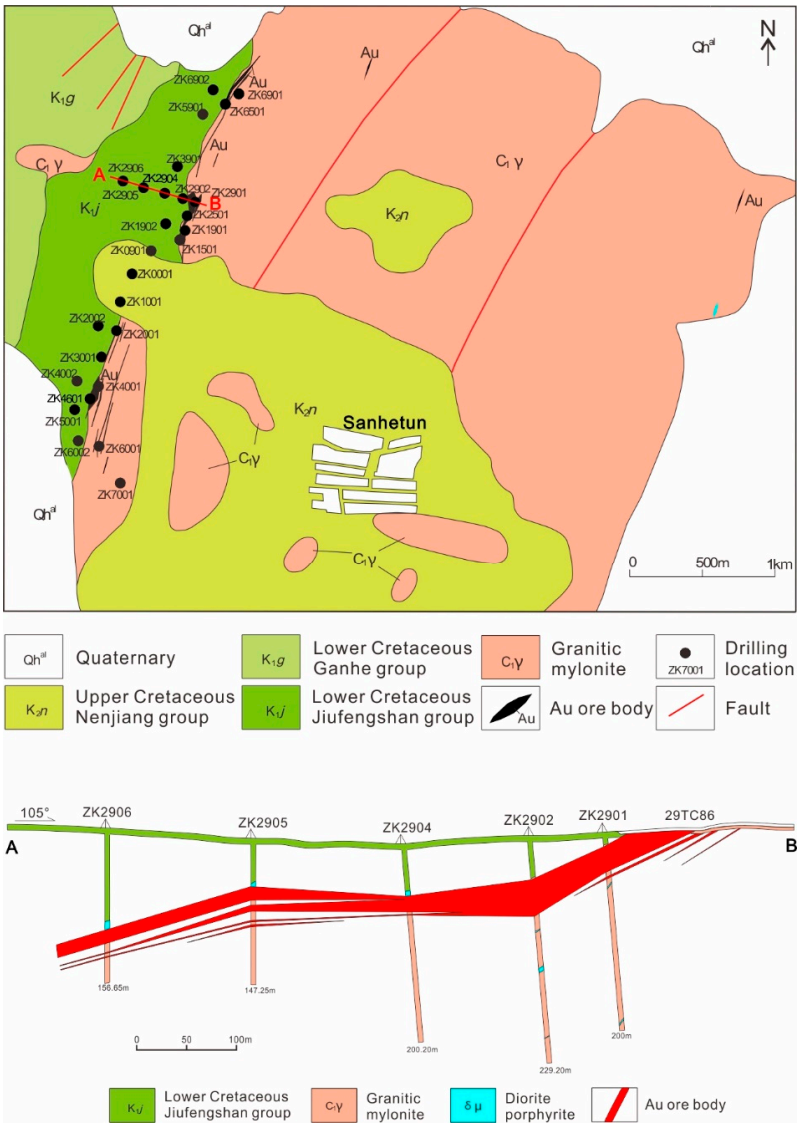

Figure 2. Geological map and cross-section of No. 29 exploration line of the Sanhetun Te–Au deposit (modified after [22]).

Up to now, three large-scale gold mineralized with pyritic alteration have been delineated in the mining area, all showing NNE-trending linear or lenticular parallel distribution. Generally, most ore bodies are 1.2 to 4.1 m thick and extend for 150–270 m in a NNE direction (15–25°), dipping to the northwest at moderate angles (40–55°). The

gold resource in the Sanhetun deposit is greater than 4 tons, with an average grade of 2.23 to 8.70 g/t [16]. The ores mainly consist of pyrite, which accounts for approximately 90% of the metallic minerals. Minor amounts of chalcopyrite, galena, sphalerite, and other minerals also occur. The main Au-bearing minerals consist of native gold and tellurides. The gangue minerals mainly consist of quartz, plagioclase, K-feldspar, biotite, sericite, chlorite, epidote, clay minerals, and minor amounts of carbonate minerals. The wall-rock alteration types mainly include silicification, sericitization, chloritization, and pyritization. Silicification and pyritization are closely related to gold mineralization (Figure 3). The NNE trend of the mineralized alteration zone is 1200 m long and 75–150 m wide in the north section; the length of the south section is 1000 m, and the width is 70–160 m.

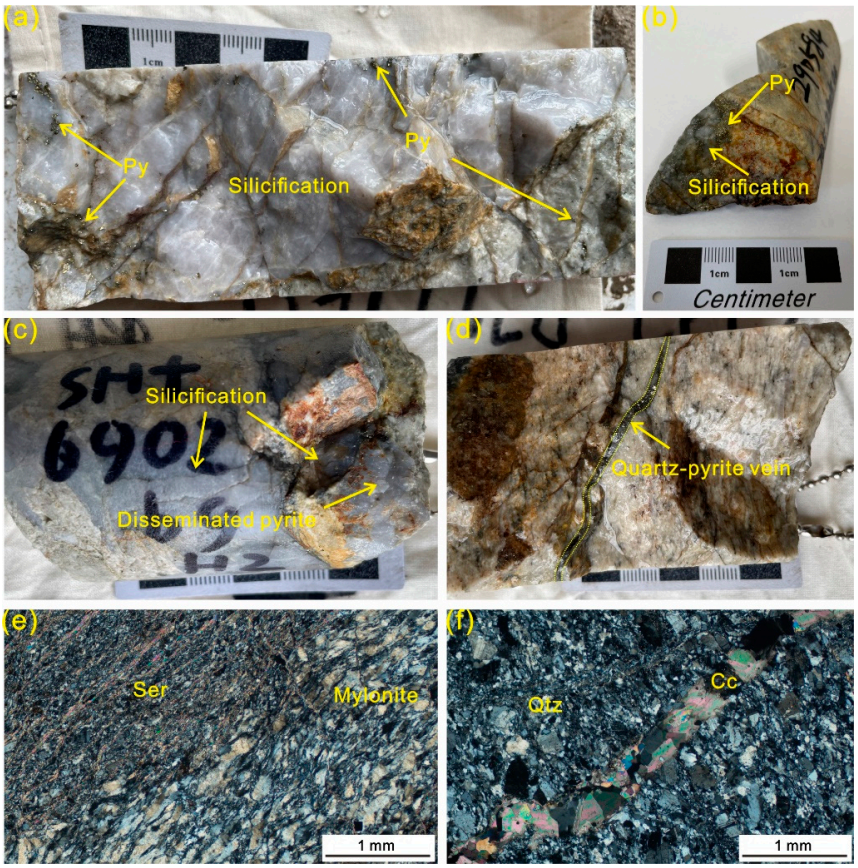

Figure 3. The main alteration types found within the Sanhetun Te–Au deposit. (**a**–**d**) Hand specimen photographs showing strong silicification accompanied by pyritization; (**e**) Reflected light photomicrographs showing sericitization mylonite; (**f**) Reflected light photomicrographs showing carbonatization wall rocks. Cc—carbonite; Py—pyrite; Qtz—quartz; Ser—sericite.

3. Materials and Methods

A total of 55 representative mineralized samples were collected from the drill cores of the No. 29 cross-section at different mining levels, which cover different mineralization stages in the Sanhetun Te–Au deposit. Polished thin sections were made from intensely pyritized ore samples to study the petrographic characteristics and primary ore textures and identify unknown minerals under the reflected–transmitted light petrographic and scanning electron microscopy (SEM). Based on a detailed microscopic observation, 20 polished thin sections were chosen to evaluate the composition of tellurides and pyrite using the TESCAN Integrated Mineral Analyzer (TIMA), electron probe microanalysis (EPMA), laser ablation inductively coupled plasma mass spectrometry (LA-ICP-MS), and femtosecond laser ablation coupled multi-collector inductively coupled plasma mass spectrometry (fsLA-MC-ICP-MS) techniques.

3.1. TIMA Analyses

Since the tellurides occur in very small grains scattered in the matrix, they were preliminarily identified by TIMA and then further investigated with SEM-EDS and EPMA analyses. TIMA (Tescan Integrated Mineral Analyzer, TESCAN ORSAY HOLDING, Shanghai, China) analyses were performed in the Institute of Geology, Chinese Academy of Geological Sciences (CAGS), Beijing, China. An automated mineralogy approach has been adopted for phase/mineral and element distribution mapping obtained by TIMA. The analyses were conducted on the thin section under dot-mapping mode with 25 kV accelerating voltage, 7.55 nA beam current, 15 mm working distance and 1 μm pixel size. The X-ray count of each point was 1000 kcps. Off-line processing software TIMA was used to identify minerals, and for data statistics and collation.

3.2. SEM Analyses

SEM observations and energy-dispersive X-ray spectroscopy (EDS) point analyses were conducted on a TESCAN MIRA3-XMU scanning electron microscope with an Oxford X-Max 20 EDS at the Research Center of Genetic Mineralogy, China University of Geosciences, Beijing. Operating conditions were a beam current of 75 nA, an accelerating voltage of 20 kV, and a working distance of 15 mm.

3.3. EPMA Analyses

Major and trace element compositions of pyrite were analyzed using a JEOL JXA-8530F electron probe microanalyzer (JEOL, Tokyo, Japan) at the State Key Laboratory for Mineral Deposits Research, Nanjing university. Operating conditions were a beam current of 20 nA, an accelerating voltage of 15 kV, and a 20 s counting time for all elements. The beam diameter was set at either 1 or 5 μm depending on the grain size being measured. The set of analyzed elements included Fe and S for major contents and Au, Ag, As, Te, Se, Cu, Pb, Zn, Co, and Ni for minor and trace element contents. The standards used were native Au, Ag, and Te; pyrite for S and Fe; bismuth selenide for Bi and Se; pentlandite for Co and Ni; arsenopyrite for As; crocoite for Pb; sphalerite for Zn; and chalcopyrite for Cu. Mean detection limits ranged from 0.01 to 0.03 wt.% for most analyzed elements. ZAF corrections were performed with proprietary JEOL software.

3.4. LA-ICP-MS Analyses

Five representative polished thin sections were analyzed using the laser ablation-inductively coupled plasma-mass spectrometer at the Yanduzhongshi Geological Analysis Laboratories Ltd., Beijing, China. Pyrite was analyzed using an Analytikjena M90 (Analytikjena, Jena, Germany) quadrupole ICPMS coupled with a 193 nm NWR193 Ar-F excimer laser for laser ablation. Ablation was performed within an atmosphere of ultra-high purity He at a flow rate of 0.9 L/min. The resulting aerosol was then mixed with Ar at a flow rate of 0.87 L/min immediately after exiting the ablation cell through a T-connector before entering the ICP [23]. For each analysis, a consistent spot diameter of 30 μm was used with a frequency of 7 Hz and an energy of approximately 2 J/cm^2 for a duration of 40 s. Prior to each analysis, a gas blank measurement was conducted for 20 s. In the analysis process, external standards were employed to plot the calibration curve. The standard reference materials BCR-2G, NIST 612, and NIST 610 were utilized for this purpose. To assess the accuracy of sulfide elements in the unknown samples, the sulfide standard MASS-1 was employed. To ensure the accuracy of the analyses, the standard reference materials were measured after every 10–15 samples. In each spot analysis, the detection limits of each element were calculated, allowing for the determination of the minimum concentration that could be reliably quantified. The mean detection limits were less than 1 ppm for most analyzed elements. The data were collected on a total of 18 elements: Au, Ag, As, Te, Bi, Se, Ge, Mo, Cd, Sb, Cu, Pb, Zn, Tl, Ti, Mn, Co, and Ni. The data processing was carried out using the ICPMSDataCal procedure.

3.5. In Situ Sulfur Isotope Analyses

Pyrite in situ S isotope analyses were conducted using a RESOlution SE laser-ablation system attached to a Thermo Fisher Scientific Neptune Plus MC-ICP-MS at Createch Testing Technology Co., Ltd., Tianjin, China. A 20–50 μm spot size was used with a 6–8 Hz repetition rate and an energy density of 6–8 J/cm^2, depending on the S contents of the samples. Helium (150 mL/min) was utilized as the carrier gas to efficiently purify aerosols from the ablation cell, and this gas was mixed with Ar (~0.8 L/min) in a T-connector before they entered into the ICP torch. The S isotopic data were obtained by static multi-collection in high-resolution mode. The Neptune MC-ICP-MS was tuned using a standard to obtain maximum sensitivity before the analyses. The Wenshan natural pyrite crystal (WS-1) was utilized as a standard. Instrumental mass discrimination was calibrated using the sample-standard bracketing method.

4. Results

4.1. Mineral Paragenetic Assemblages

Based on the mineral assemblage, structures, and crosscutting relationships, five mineralization stages have been identified as follows: the pyrite–quartz stage (I), quartz–pyrite stage (II), gold–telluride–polymetallic sulfide stage (III), telluride–pyrite stage (IV), and carbonate stage (V). The stage (I) is characterized by milky quartz and minor disseminated pyrite (Py1) that displays euhedral to subhedral coarse-grained morphology (Figure 4d). The stage (II) is characterized by fine-grained pyrite veinlets that crosscut Py1 (Figure 4e). A small amount of calcite veins occurs in this stage. The ore stage (III and IV) is characterized by anhedral aggregated pyrite (Py3 and Py4). Stage III and IV are the most important Te–Au mineralization stages. Native gold, tetradymite, galena, and chalcopyrite commonly coexist with Py3 (Figure 4f–h). A significant amount of tetradymite occurs within Py4 (Figure 4i). The main mineral assemblages of each stage are illustrated in Figure 5.

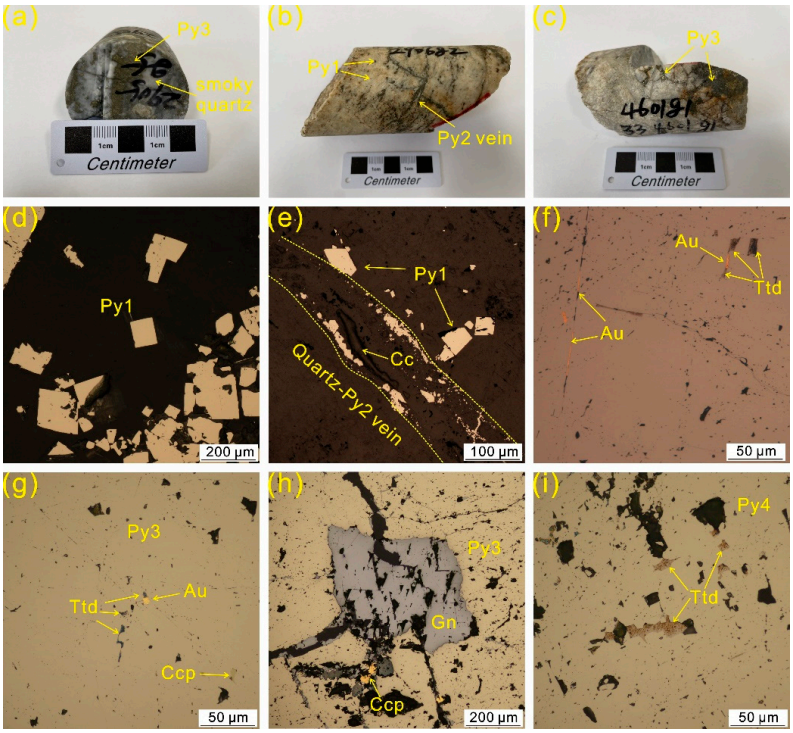

Figure 4. Ore features and photomicrographs of different mineralization stages from the Sanhetun Te–Au deposit. (**a**–**c**) Representative hand specimens of ore; (**d**) euhedral cubic Py1; (**e**) Py2 veinlets crosscut the euhedral Py1; (**f**,**g**) native gold coexists with tetradymite within Py3; (**h**) polymetallic sulfide in the main ore stage; (**i**) tetradymite occurs within Py4. Au—native gold; Cc—calcite; Ccp—chalcopyrite; Py—pyrite; Gn—galena; Ttd—tetradymite.

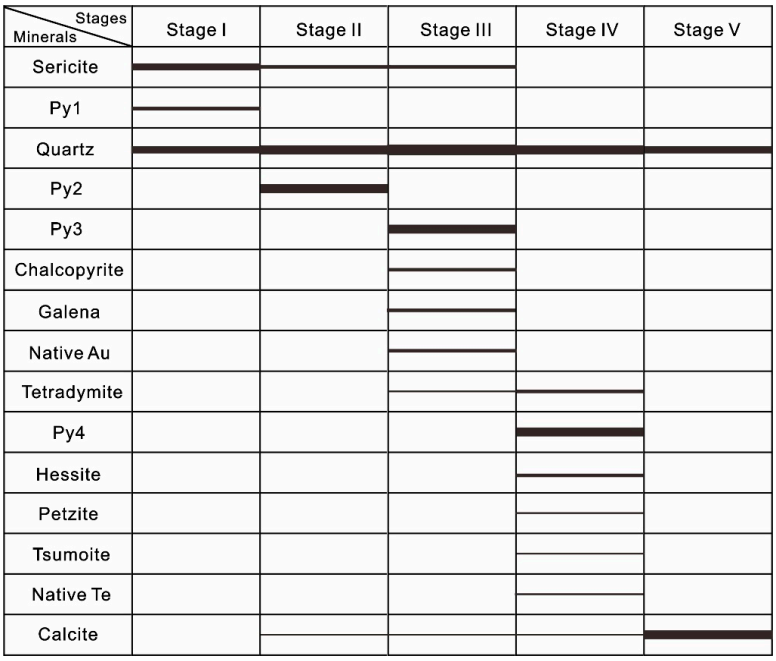

Figure 5. Paragenetic sequence of the major minerals in the Sanhetun Te–Au deposit. Note: The width of the lines represents the relative abundance of minerals.

4.2. Telluride Mineralogy

The TIMA results show that a number of tellurides occur in the Sanhetun Te–Au deposit, including native tellurium, tetradymite, tsumoite, hessite, and petzite (Figure 6). These tellurides commonly occur along the fracture or grain boundary of Py4 or as irregular patches within Py4 (Figure 4i). Among them, tetradymite has a close spatial relationship with native gold within Py3 (Figure 4f,g). The detailed description of tellurides is as follows.

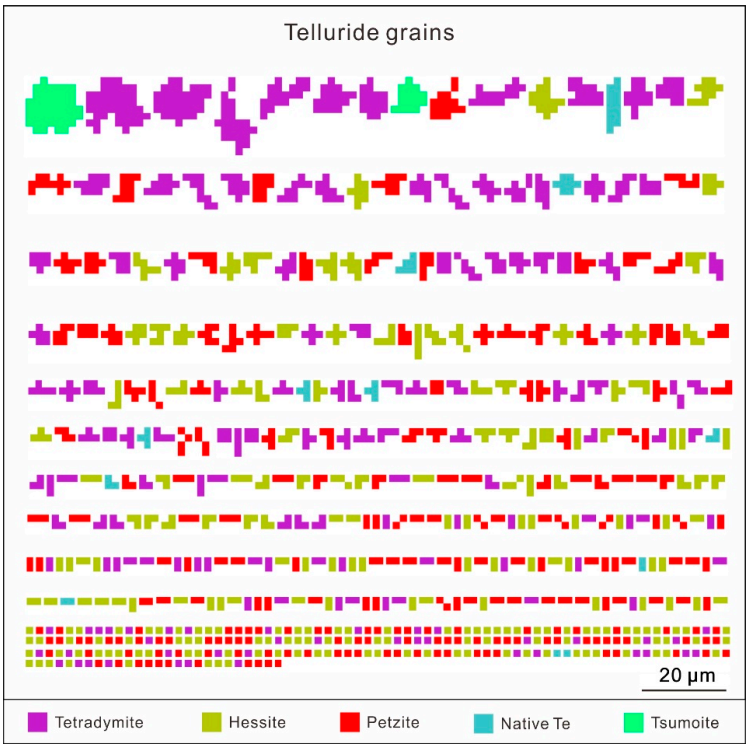

Figure 6. Independent tellurium-bearing mineral grains identified by TIMA in the Sanhetun Te–Au deposit.

Tetradymite [Bi_2Te_2S] is the most abundant telluride in the Sanhetun Te–Au deposit (Figure 6). Individual grains are commonly anhedral, ranging in size from 6 to 55 μm. Of note, tetradymite is spatially associated with native gold (Figure 4f,g).

Hessite [Ag_2Te] is the next most abundant precious metal telluride and commonly coexists with petzite and galena. It is usually present as fine-grained and irregular patches enveloped within the pyrite (Figure 7c–e).

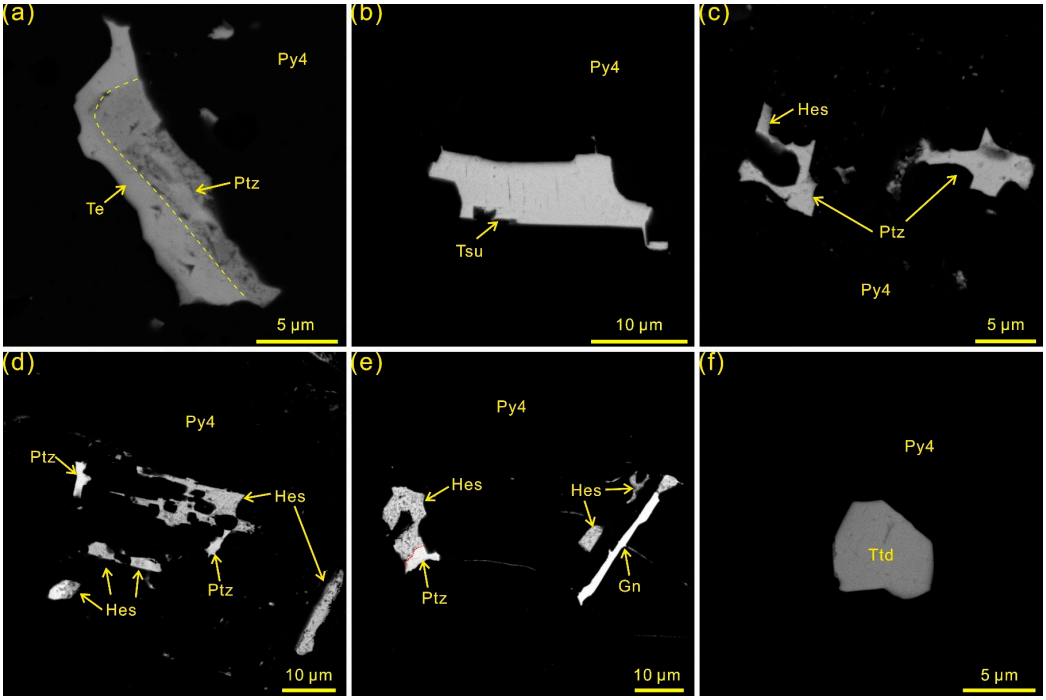

Figure 7. BSE images of tellurides from the Sanhetun Te–Au deposit. (**a**) Native Te coexists with petzite; (**b**) tsumoite occurs alone within pyrite; (**c**–**e**) hessite commonly coexists with petzite and galena; (**f**) tetradymite occurs alone within pyrite. Gn—galena; Hes—hessite; Ptz—petzite; Py—pyrite; Te—native tellurium; Tsu—tsumoite.

Petzite [Ag_3AuTe_2] is less abundant than tetradymite and hessite, which has a close relationship with native tellurium and hessite (Figure 7a,c–e).

Native tellurium is rare in our sample set, which has an intimate association with petzite. Individual grains are anhedral, ranging in size from 5 to 20 μm (Figure 7a).

Tsumoite [BiTe] is scarce and commonly occurs isolated. Grain size is approximately 10 to 20 μm (Figure 7b).

4.3. Pyrite Composition

A total of 71 EPMA spot analyses were conducted on pyrite grains from different stages in the Sanhetun Te–Au deposit. The complete dataset of pyrite major elements is presented in Supplementary Table S1. The summary of major elements is listed in Table 1. The data show that all stages of pyrite have similar S and Fe contents, which are 52.54~53.98 wt.% and 46.03~47.31 wt.%, respectively. Gold and Ag are enriched in Py3, which has the highest concentrations of Au and Ag in comparison to Py1, Py2, and Py4, up to 0.13 and 0.17 wt.%. Arsenic concentrations are commonly low in all pyrite grains, less than 0.05 wt.%, indicating the As-poor pyrite from the Sanhetun deposit. Other elements, such as Cu, Pb, Zn, Co, Ni, and Se, are detected in trace contents, as in from tenths to thousands ppm.

Table 1. The summary of major element compositions of pyrite from the different stages in the Sanhetun Te–Au deposit (all values in wt.%).

	Py1			**Py2**			**Py3**			**Py4**		
	N = 19			**N = 23**			**N = 14**			**N = 14**		
	Min	**Mean**	**Max**	**Min**	**Mean**	**Max**	**Min**	**Mean**	**Max**	**Min**	**Mean**	**Max**
S	52.64	53.19	53.45	53.46	53.65	53.93	52.54	53.39	53.98	52.76	53.55	53.91
Fe	46.03	46.64	47.14	46.29	46.75	47.14	46.37	46.69	47.31	46.15	46.56	47.05
Au	0.00	0.00	0.02	0.00	0.00	0.02	0.00	0.03	0.08	0.03	0.06	0.13
Ag	0.00	0.02	0.06	0.00	0.01	0.07	0.00	0.01	0.07	0.00	0.04	0.17
Te	0.00	0.02	0.10	0.00	0.01	0.05	0.00	0.02	0.08	0.00	0.03	0.10
Se	0.00	0.01	0.08	0.00	0.01	0.05	0.00	0.01	0.05	0.00	0.01	0.03
As	0.00	0.01	0.03	0.00	0.00	0.04	0.00	0.01	0.04	0.00	0.01	0.05
Cu	0.00	0.01	0.04	0.00	0.02	0.08	0.00	0.00	0.03	0.00	0.01	0.03
Pb	0.00	0.04	0.20	0.00	0.03	0.14	0.00	0.03	0.10	0.00	0.05	0.14
Zn	0.00	0.03	0.13	0.00	0.02	0.08	0.00	0.05	0.08	0.00	0.03	0.08
Co	0.00	0.04	0.09	0.00	0.03	0.08	0.01	0.05	0.15	0.00	0.04	0.08
Ni	0.00	0.00	0.01	0.00	0.01	0.08	0.00	0.02	0.07	0.00	0.00	0.03
Total	98.67	100.01	101.35	99.75	100.54	101.76	98.92	100.31	102.04	98.94	100.39	101.80
S(apfu)	2.03	2.01	1.98	2.02	2.00	1.98	2.02	2.00	1.98	2.03	2.01	1.99
Fe(apfu)	1.00	1.00	1.01	0.99	1.00	1.00	1.01	1.00	1.00	1.00	0.99	1.00

A total of 31 LA-ICP-MS trace element spot analyses were performed on pyrite from the Sanhetun Te–Au deposit (Supplementary Table S2), including ten spots on Py1, ten spots on Py2, six spots on Py3, and five spots on Py4. The summary of trace elements is listed in Table 2. The results reveal distinct trace element abundance in all stages of pyrite (Figure 8). Py1 displays the lowest contents of detected trace elements; except for Co and Ni, the trace element contents of Py1 are often at or below the detection limits. Py2 preserves slightly higher As contents (59.24~1784.14 ppm) compared to Py1 (0~12.85 ppm), Py3 (0~6.01 ppm, except for one outlier), and Py4 (3.33~7.44 ppm). In addition to As, Py2 also shows relatively higher contents of elements such as Mo (163.94~625.39 ppm), Sb (4.65~53.07 ppm), and Mn (6.60~152.54 ppm). The main-ore stage Py3 has the highest Au (0.36~440.79 ppm), Ag (1.93~1758.18 ppm), Te (17.60~2801.51 ppm), Bi (0.61~196.02 ppm), and Pb (15.79~8651.72 ppm) contents. The Co contents of Py3 are very low, varying from 0.07 to 0.43 ppm except for one outlier (46.61 ppm). Compared to Py3, the post-ore stage Py4 shows relatively lower contents of elements, including Te, Bi, Au, and Ag.

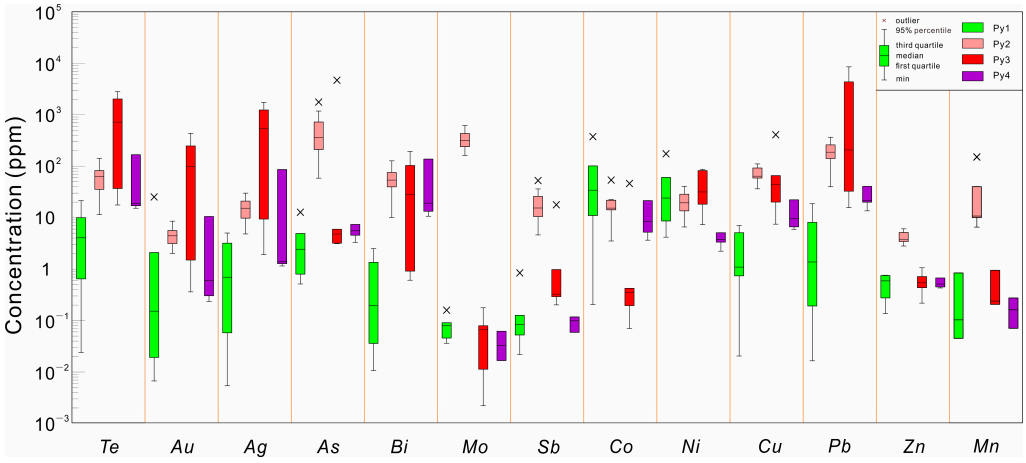

Figure 8. Box and whisker diagrams of trace element contents of the four generations of pyrite of the Sanhetun Te–Au deposit.

Table 2. The summary of trace element compositions of pyrite from the different stages in the Sanhetun Te–Au deposit (all values in ppm).

	Py1 N = 9			**Py2 N = 10**			**Py3 N = 7**			**Py4 N = 5**		
	Min	**Mean**	**Max**	**Min**	**Mean**	**Max**	**Min**	**Mean**	**Max**	**Min**	**Mean**	**Max**
Ti	0.93	2.98	6.17	4.66	164.80	691.12	1.06	2.36	5.88	1.15	1.80	2.25
Mn	0.00	0.18	0.85	6.60	38.77	152.54	0.00	0.29	0.95	0.00	0.14	0.28
Co	0.21	96.24	380.43	3.55	20.87	54.32	0.07	10.56	46.61	3.67	10.97	21.68
Ni	0.00	47.63	176.43	6.65	22.19	40.89	7.35	44.72	87.78	2.25	3.82	5.11
Cu	0.00	2.24	7.12	36.67	72.80	111.99	7.54	118.12	414.41	5.98	12.41	22.39
Zn	0.14	0.49	0.77	2.83	4.24	6.12	0.22	0.59	1.07	0.43	0.55	0.68
Ge	4.23	4.67	5.16	4.33	4.70	5.17	4.13	4.80	5.72	4.09	4.61	5.09
As	0.00	3.59	12.85	59.24	627.81	1784.14	0.00	1058.53	4752.33	3.33	5.39	7.44
Se	0.00	1.42	3.34	0.00	1.82	4.02	0.19	1.08	4.21	2.00	3.12	4.39
Mo	0.04	0.08	0.16	163.94	368.91	625.39	0.00	0.07	0.18	0.00	0.03	0.06
Ag	0.00	1.46	5.08	4.87	15.99	30.27	1.93	689.57	1758.18	1.16	26.13	87.08
Cd	0.00	0.05	0.19	0.26	1.48	3.33	0.00	1.45	4.83	0.00	0.04	0.11
Sb	0.00	0.19	0.85	4.65	21.70	53.07	0.20	4.31	18.00	0.00	0.06	0.12
Te	0.02	6.66	21.36	11.43	68.38	142.43	17.60	1115.65	2801.51	15.23	62.32	166.87
Au	0.01	4.98	25.49	2.03	4.92	8.59	0.36	159.01	440.79	0.24	3.39	10.62
Tl	0.00	0.01	0.05	0.28	1.39	3.29	0.00	0.03	0.08	0.00	0.01	0.02
Bi	0.00	0.72	2.53	10.15	58.08	128.55	0.61	70.43	196.02	10.73	53.43	139.45
Pb	0.02	4.78	18.90	40.36	201.98	369.50	15.79	2489.75	8651.72	13.66	26.75	40.93

4.4. In Situ Sulfur Isotopic Composition

A total of 35 spots were analyzed in situ for sulfur isotopic compositions by fsLa-MC-ICP-MS. The S isotopic compositions of the Sanhetun pyrites are presented in Table 3 and illustrated in Figure 9. The $\delta^{34}S$ values show a wide range of variation from −5.69 to +14.43‰ for the pyrite from the Sanhetun Te–Au deposit with up to a 20.12‰ difference, indicating that the sulfur isotopic composition of ore forming fluids is heterogeneous. Py1 has slightly negative $\delta^{34}S$ values ranging from −1.20 to −0.57‰ (mean = −0.8, n = 7). Py2 is characterized by the most variable positive $\delta^{34}S$ values ranging from 4.67 to 14.43‰ (mean = 8.23, n = 10). Py2 has two populations. The first population ranges from 4.67 to 6.88, with a mean of 5.83. The second one ranges from 10.78 to 14.43, with a mean of 11.83. Py3 displays $\delta^{34}S$ values ranging from −5.69 to 0.19‰ (mean = −2.89, n = 10). Py3 also has two populations. The first population ranges from −5.69 to −4.38, with a mean of −5.07. The second one ranges from −1.09 to 0.19, with a mean of −0.71. Py4 has a narrow range of $\delta^{34}S$ values, ranging from 2.66 to 3.86‰ (mean = 3.41, n = 8).

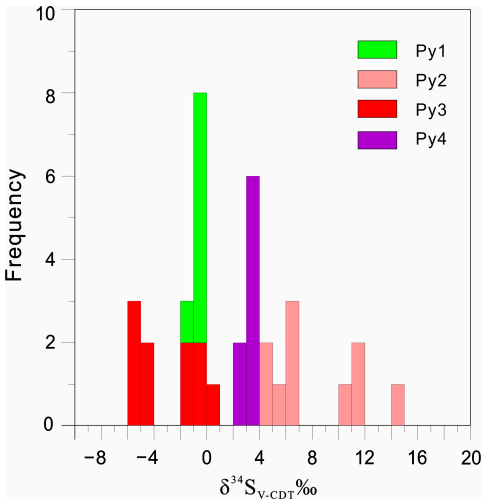

Figure 9. Sulfur isotopic compositions of the four generations of pyrite of the Sanhetun Te–Au deposit.

Table 3. Sulfur isotopic compositions of pyrite from the Sanhetun Te–Au deposit.

Stage	Sample No.	$\delta^{34}S_{V\text{-}CDT}$ (‰)
Py1	ZK2904g7-1-1	−0.85
Py1	ZK2904g7-1-2	−0.66
Py1	ZK2904g7-1-3	−1.20
Py1	ZK2904g7-1-4	−0.65
Py1	ZK2904g7-1-5	−0.57
Py1	ZK2904g7-1-6	−0.69
Py1	ZK2904g7-1-7	−0.95
Py2	ZK2905g5-1-1	14.43
Py2	ZK2905g5-1-2	11.09
Py2	ZK2905g5-1-3	5.33
Py2	ZK2905g5-1-4	6.59
Py2	ZK2905g5-1-5	6.88
Py2	ZK2905g5-1-6	11.03
Py2	ZK2905g5-1-7	6.78
Py2	ZK2905g5-1-8	4.75
Py2	ZK2905g5-1-9	4.67
Py2	ZK2905g5-1-10	10.78
Py3	ZK2905g3-1	−0.74
Py3	ZK2905g3-2	−5.69
Py3	ZK2905g3-3	−4.38
Py3	ZK2905g3-4	−5.44
Py3	ZK2905g3-5	−5.16
Py3	ZK2905g3-6	−4.69
Py3	ZK2905g3-7	−0.89
Py3	ZK2905g3-8	−1.09
Py3	ZK2905g3-9	0.19
Py3	ZK2905g3-10	−1.03
Py4	ZK1001g2-1-1	2.90
Py4	ZK1001g2-1-2	2.66
Py4	ZK1001g2-1-3	3.05
Py4	ZK2905g5-1	3.62
Py4	ZK2905g5-2	3.65
Py4	ZK2905g5-3	3.86
Py4	ZK2905g5-4	3.76
Py4	ZK2905g5-5	3.78

5. Discussion

5.1. Trace Element Distribution in Pyrite

Previous studies [24–27] have highlighted that pyrite can incorporate different types of trace elements in different forms. These elements commonly occur as a solid solution dissolved in the pyrite structure, visible mineral inclusions, or invisible nanoparticles dispersed within the pyrite. Here, we mainly concentrated on the distribution and occurrence of As, Au, and Te in different stages of pyrite from the Sanhetun Te–Au deposit. Arsenic is one of the most common trace elements in pyrite, which can serve as either $As^{2+/3+}$ replacing Fe^{2+} or as As^{-} replacing S^{-} during isomorphic substitution or as amorphous As^{0} nanoparticles [28–32]. The EPMA data suggest that pyrite within the Sanhetun Te–Au deposit is As-poor (<0.1 wt%). The LA-ICP-MS data also show that all types of pyrite are deficient in As, even though Py2 has a slightly higher As content. Previous studies show that As and Au have coupled geochemistry in pyrite from multiple types of gold deposits [33,34]. However, the As–Au binary diagram shows that there is no clear correlation between the concentrations of Au and As (Figure 10a). This diagram also shows that the data points of Py1, Py2, and Py4 fall below the Au saturation line, indicating that the dominant form of gold is found as a solid solution. The data points of Py3, however, fall in the area above the line, suggesting that Au occurs as Au nanoparticles and submicrometer-sized Au-bearing mineral inclusions. According to [28], the incorporation of Te and Au in pyrite shares a similar mechanism, and the authors further hypothesized that the Au saturation line

may also be applicable to Te. In the As–Te binary diagram (Figure 10b), the data points of the different stages of pyrite mostly plot above the Au saturation line, indicating that the majority of the tellurium of the Sanhetun Te–Au deposit occurs as mineral inclusions. This interpretation is supported by the LA-ICP-MS time-resolved depth profile (Figure 11). Py1 and Py2 commonly have discontinuous or smooth profiles for Te and Au, implying that the Te and Au are mainly distributed as a solid solution within Py1 and Py2 (Figure 11a,b). With regard to Py3 and Py4, the LA-ICP-MS profiles for Au, Bi, and Te are generally synchronously ragged, indicating the presence of Te–Bi–Au inclusions (Figure 11c,d). This is further supported by the binary plots of the trace elements of pyrites, which show a remarkably positive correlation between Te, Bi, and Au (Figure 10c–f). According to [25], the occurrence of nanoparticles of Au–telluride in As-free pyrite was confirmed by direct observation using transmission electron microscopy (TEM). These nanoparticles are able to contribute to a large proportion of the Au budget in As-free pyrite.

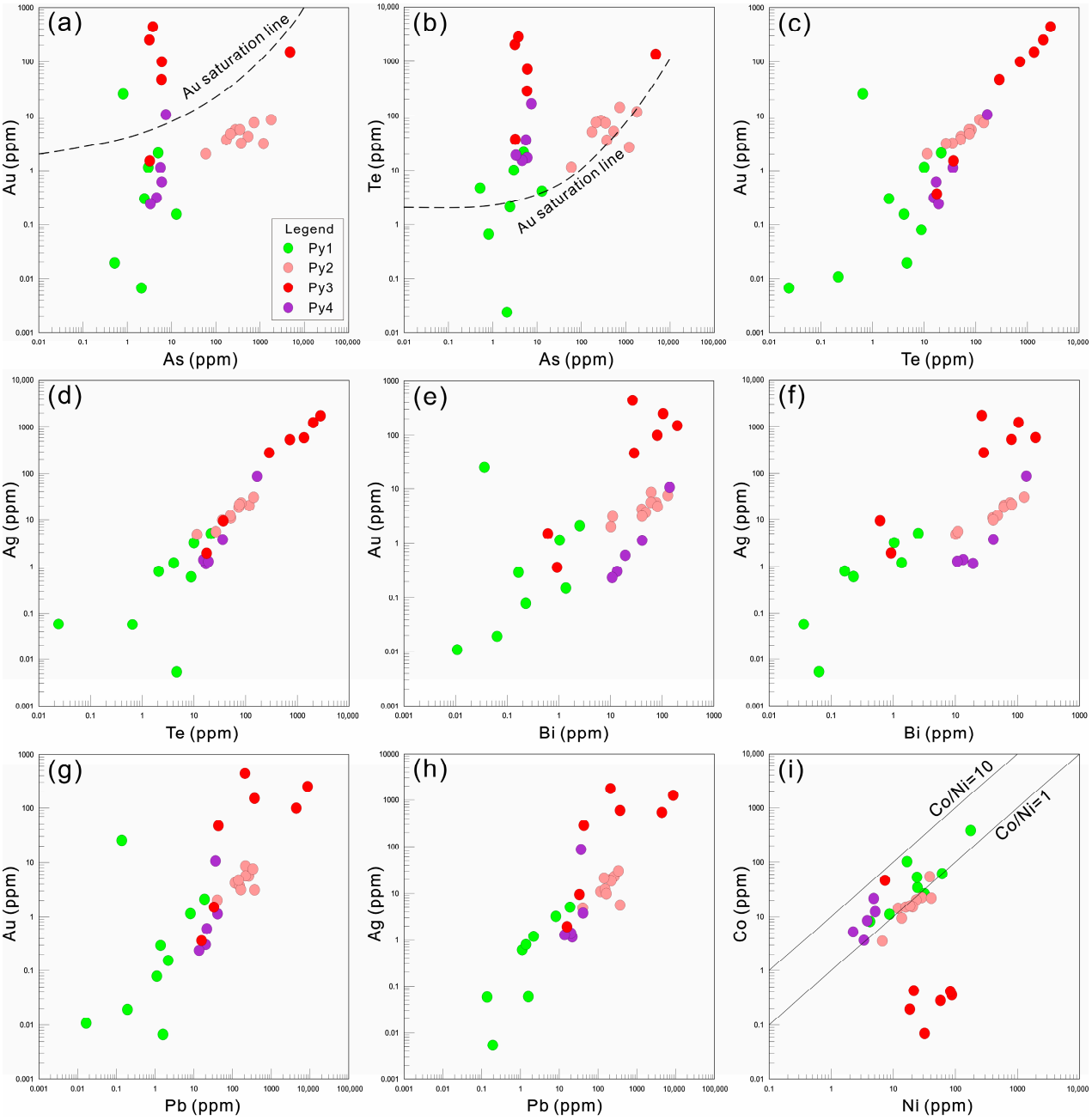

Figure 10. *Cont.*

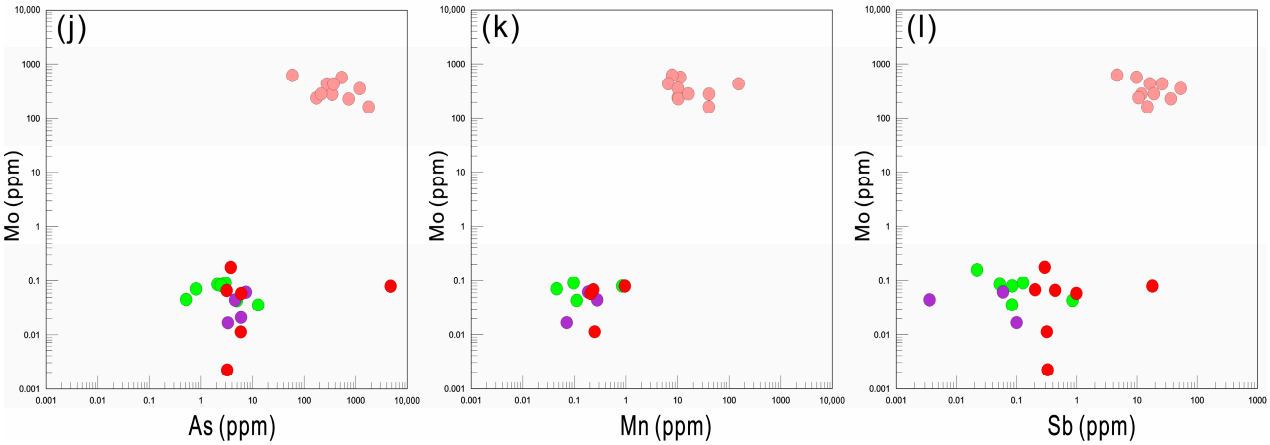

Figure 10. Bivariate plots of trace elements in different types of pyrite from the Sanhetun Te–Au deposit. Au saturation line after [34]. (**a**) As–Au, (**b**) As–Te, (**c**) Te–Au, (**d**) Te–Ag, (**e**) Bi–Au, (**f**) Bi–Ag, (**g**) Pb–Au, (**h**) Pb–Ag, (**i**) Ni–Co, (**j**) As–Mo, (**k**) Mn–Mo, (**l**) Sb–Mo. The dashed lines in (**a**,**b**) show the Au and Te solubility limits as a function of As in pyrite after [28,32].

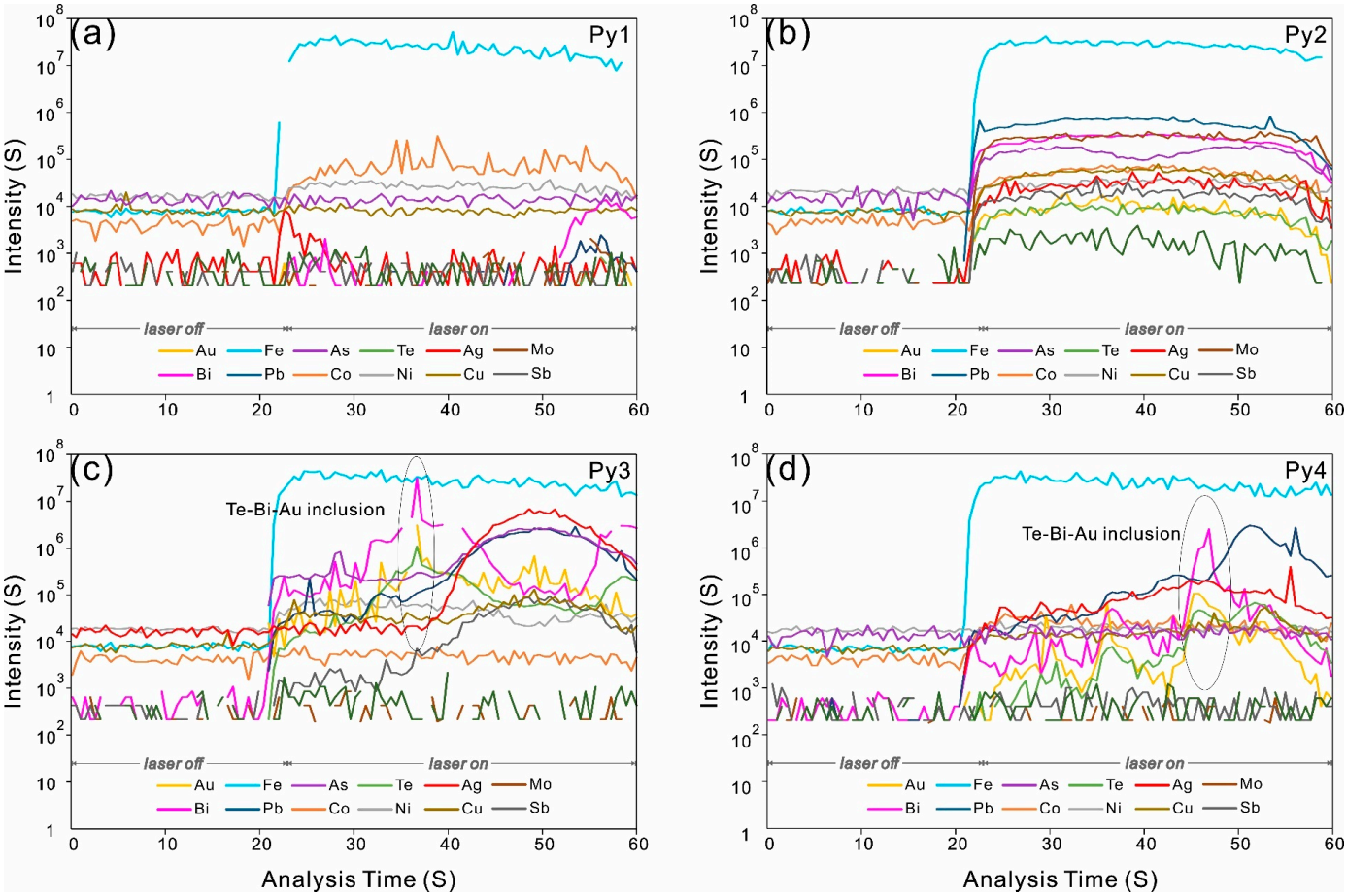

Figure 11. Representative LA-ICP-MS time-resolved depth profiles for different types of pyrite from the Sanhetun Te–Au deposit. (**a**,**b**) Py1 and Py2 LA-ICP-MS time-resolved depth profiles displaying Te and Au solid solutions; (**c**,**d**) Py3 and Py4 LA-ICP-MS time-resolved depth profiles showing Te–Bi–Au inclusions.

5.2. Genesis of Pyrite

The trace elements and S isotopes of pyrite can provide critical information to understand the source and evolution of the ore-forming fluids [35–37]. Based on the mineral assemblage, crosscutting relationships, trace elements, and S isotopes of pyrite, four types of pyrite have been recognized from the Sanhetun Te–Au deposit.

The pre-ore stage Py1 is significantly deficient in Au, Ag, As, Te, and other trace elements except for Co and Ni and has a narrow range of $\delta^{34}S$ values from −1.20 to −0.57‰. The relatively uniform $\delta^{34}S$ values of Py1 indicate that the ore-forming fluids were probably derived from a homogeneous sulfur source. The $\delta^{34}S$ values close to 0 suggest that magmatic sulfur could generate the $\delta^{34}S$ range for Py1. There is little Au and Te to precipitate in this stage.

Py2 exhibits distinguishable features of trace elements and $\delta^{34}S$ composition in comparison with the other generations of pyrite. It features relatively high contents of As, Mo, Sb, Zn, and Mn (Figure 10j–l) with a wide range of $\delta^{34}S$ values from 4.67 to 14.43‰ (mean = 8.23, n = 10). The characteristics of Py2 indicate that the remarkably positive $\delta^{34}S$ was contributed by the wall rock mylonite. The two populations of $\delta^{34}S$ values may be attributed to the mixing of different proportions of wall rock. In addition, a previous study shows that the mylonite has relatively high concentrations of Te (0.17 ppm) and Au (0.02 ppm) [38], indicating that the mylonite might supply part of the Te and Au in the formation of the Sanhetun Te–Au deposit.

The main-ore stage Py3 contains the highest Au, Ag, Te, and Bi concentrations with a range of negative $\delta^{34}S$ values from −5.69 to 0.19‰ (mean = −2.89, n = 10). The negative $\delta^{34}S$ values could be ascribed to several reasons, including a biogenic or sedimentary sulfur origin and isotope fractionation driven by high oxygen fugacity and boiling of magmatic-derived fluids [39,40]. Among these reasons, sulfur isotope fractionation under high oxygen fugacity is the most possible mechanism causing the negative $\delta^{34}S$ values of pyrite. Tellurium is widely recognized for its high solubility in ore-forming fluids under high oxygen fugacity conditions; however, under more reduced conditions, its solubility experiences a significant decrease [30,41,42]. This is in line with the highest concentrations of Te in Py3. In addition, the two populations of $\delta^{34}S$ values may be ascribed to the fluctuation of oxygen fugacity. Previous studies have suggested that the ratio of Bi/Te (+S, Se) in phases belonging to the tetradymite group can serve as an indicator of the redox conditions of ore-forming fluids. Phases with a Bi/Te (+S, Se) ratio greater than 1 are typically associated with reduced conditions, whereas those with a Bi/Te (+S, Se) ratio less than 1 indicate oxidized conditions [43,44]. The Sanhetun Te–Au deposit contains abundant tetradymite (Bi_2Te_2S), which has a Bi/Te (+S, Se) ratio < 1, indicating that the ore-forming fluids were in oxidizing conditions.

Py4 contains relatively low Te and Au with slightly positive $\delta^{34}S$ values ranging from 2.66 to 3.86‰. Such $\delta^{34}S$ values are similar to the usual estimate of $\delta^{34}S$ values for magmatic sulfur [45], implying that magmatic sulfur could generate the $\delta^{34}S$ range for Py4. The Co/Ni ratios of Py4 are generally >1, further supporting that ore-forming fluids are magmatic fluids. Petrographic observation shows that the majority of telluride coexists with Py4. However, Py4 commonly lacks Au, indicating that the majority of Au is deposited in Py3. The precipitation of a large amount of sulfide consumed large amounts of sulfur, leading to the increase of fTe_2/fS_2. The elevated fTe_2/fS_2 ratios give rise to the deposition of telluride in Py4, especially native tellurium, which reflects the high Te fugacity of the ore-forming fluids.

5.3. Enrichment Mechanism of Au

The mechanism of Au enrichment is crucial to understanding the genesis of gold deposits. Several mechanisms have been proposed by previous studies, including a rapid decrease in Au solubility [46], coupled dissolution–reprecipitation (CDR) [47], electrochemical accumulation of Au [48,49], fault-valve processes [50], and the low melting chalcophile elements (LMCE) melt collector model [51–56]. The enrichment mechanism of Au in the

Sanhetun is still unclear since it is a newly discovered gold deposit. The LMCE melt collector model is probably the most effective in the Sanhetun deposit, as shown by the several Te–Bi minerals recognized, particularly tetradymite, which has a close relationship with native gold (Figure 4f,g). Both Te and Bi are, in fact, LMCE, and the role they play in scavenging Au and other precious metals has been widely researched [47,53,54,57–60]. A highly efficient mechanism for Au enrichment is the liquid bismuth collector model, based on theoretical calculations and experiments [52,53]. On the other hand, there are relatively few convincing studies proving the role of tellurium as an Au scavenger. According to [54,55], the Te-rich melts can scavenge gold from Au-undersaturated ore-forming fluids, leading to the formation of Au-enriched melts. This mechanism could be envisaged in the Sanhetun deposit, where native gold is generally intergrown with tetradymite (Figure 4f,g). Moreover, the binary plots of trace elements of pyrites (Figure 10c,e) show a positive correlation between Te, Bi, and Au, indicating that they have strong geochemical affinity. Thus, Te and Bi may play a critical role in governing Au enrichment. Of note, Au and Pb also show a positive correlation in the binary plots (Figure 10g). This may suggest that the Au mineralizing stage is coeval with sulfide-friendly elements, supporting the role of sulfur for Au extractions as melt droplets. Hence, the presence of sulfur in the native gold and tetradymite mineral assemblage may have also played a critical role as Te–Bi–S melts, which will efficiently scavenge Au from ore-forming fluids, even undersaturated [52,53]. This scavenging process results in the formation of nano- to micrometer-scale Au–Te–Bi–S melt droplets. The cooling of micrometer-scale melt droplets caused the precipitation of the native gold and tetradymite identified in the Sanhetun deposit. Nanometer-scale melt droplets were also trapped within pyrite, as suggested by the Au–Te–Bi spiky signals in the time-resolved profiles of Py3 and Py4 (Figure 11c,d). These sets of evidence suggest that the formation of the Sanhetun Te–Au deposit is closely linked to the Au-enrichment from the formation of Te–Bi–S melts in Au-undersaturated mineralizing fluids.

6. Concluding Remarks

(1) Five species of telluride were recognized in the Sanhetun Te–Au deposit: native Te, tetradymite, tsumoite, hessite, and petzite. Tetradymite commonly has a close relationship with native gold.
(2) Four stages of pyrite are identified by their morphology, mineral assemblage, and elemental and sulfur isotopic compositions. The in situ trace elements show that the ore-forming fluids underwent an increase of fTe_2 and fTe_2/fS_2, which gave rise to the precipitation of telluride.
(3) Tellurium occurs as a lattice-bond in Py1 and Py2 and Te–Bi–Au submicroscopic inclusions concealing in Py3 and Py4. Gold is mainly present as visible gold and, subordinately, as invisible gold, which occurs as Te–Bi–Au submicroscopic inclusions.
(4) Gold enrichment of the Sanhetun Te–Au deposit might be attributed to the existence of Te–Bi–S melts, which can act as an important gold scavenger in the Au-undersaturated ore-forming fluids.

Supplementary Materials: The following supporting information can be downloaded at: https://www.mdpi.com/article/10.3390/min14101014/s1, Table S1: EMPA analyses of pyrite grains from the different stages in the Sanhetun Te-Au deposit (all values in wt. %); Table S2: LA-ICP-MS analyses of pyrite grains from the different stages in the Sanhetun Te-Au deposit (all values in ppm).

Author Contributions: Investigation, M.Z., C.L. and H.G.; data curation, K.X. and G.Z.; writing—original draft preparation, M.Z.; writing—review and editing, J.S.; funding acquisition, C.L.; writing—review and editing, M.S. All authors have read and agreed to the published version of the manuscript.

Funding: This research was funded by Major Research Plan of National Natural Science Foundation of China (Grant No. 92062219) and Heilongjiang Province Natural Science Foundation of China (Grant No. LH2023D028).

Data Availability Statement: The data presented in this study are available.

Acknowledgments: We greatly thank anonymous reviewers and editors for the constructive comments that helped to improve this paper.

Conflicts of Interest: The authors declare no conflict of interest.

References

1. Gao, R.; Xue, C.; Lü, X.; Zhao, X.; Yang, Y.; Li, C. Genesis of the Zhengguang gold deposit in the Duobaoshan ore field, Heilongjiang Province, NE China: Constraints from geology, geochronology and S-Pb isotopic compositions. *Ore Geol. Rev.* **2017**, *84*, 202–217. [CrossRef]
2. Liu, J.; Li, Y.; Zhou, Z.; OuYang, H. The Ordovician igneous rocks with high Sr/Y at the Tongshan porphyry copper deposit, satellite of the Duobaoshan deposit, and their metallogenic role. *Ore Geol. Rev.* **2017**, *86*, 600–614. [CrossRef]
3. Suo, Q.; Shen, P.; Li, C.; Feng, H.; Chu, X. Mineral chemistry and apatite Sr isotope signatures record overprinting mineralization in the Duobaoshan porphyry Cu deposit, Heilongjiang Province, NE China. *Ore Geol. Rev.* **2023**, *162*, 105718. [CrossRef]
4. Chen, J.; Wang, K.; Cai, W.; Geng, J.; Xue, H.; Wang, X. Fluid evolution and genesis of the Sankuanggou Fe -Cu skarn deposit, Duobaoshan ore field, Northeast China: Evidence from fluid inclusions and H-O-S-Pb isotopes. *J. Geochem. Explor.* **2023**, *252*, 107251. [CrossRef]
5. Yang, H.; Ma, W.L.; Cai, W.Y.; Wang, K.Y.; Sun, F.Y.; Wang, J.H.; Zhou, H.Y.; Kou, B.Y. Metallogenic epoch and tectonic setting of the Xiaoduobaoshan Fe-Cu deposit in Heilongjiang Province, China: Evidence from petrogeochemistry, zircon U-Pb geochronology and Hf isotopic compositions (in Chinese with English abstract). *Acta Petrol. Sin.* **2020**, *36*, 856–870.
6. Zhai, D.G.; Williams-Jones, A.E.; Liu, J.J.; Tombros, S.F.; Cook, N.J. Mineralogical, Fluid Inclusion, and Multiple Isotope (H-O-S-Pb) Constraints on the Genesis of the Sandaowanzi Epithermal Au-Ag-Te Deposit, NE China. *Econ. Geol.* **2018**, *113*, 1359–1382. [CrossRef]
7. Zhang, M.; Shen, J.; Santosh, M.; Li, C.; Liu, H.; Yu, H.; Kamoto, M.; Du, B.; Liu, J. Tellurium and Gold enrichment aided by melts and pyrite crystallization kinetics: Insights from the Yongxin gold deposit, Northeast China. *Ore Geol. Rev.* **2023**, *156*, 105370. [CrossRef]
8. Li, C.L.; Li, L.; Yuan, M.W.; Alam, M.; Li, S.R.; Santosh, M.; Deng, C.Z.; Liu, H.; Xu, G.Z. Study on pyrite thermoelectricity, ore-forming fluids and H-O-Rb-Sr isotopes of the Yongxin gold deposit, Central Asian Orogenic Belt: Implications for ore genesis and exploration. *Ore Geol. Rev.* **2020**, *121*, 103568. [CrossRef]
9. Yuan, M.W.; Li, S.R.; Li, C.L.; Santosh, M.; Alam, M.; Zeng, Y.J. Geochemical and isotopic composition of auriferous pyrite from the Yongxin gold deposit, Central Asian Orogenic Belt: Implication for ore genesis. *Ore Geol. Rev.* **2018**, *93*, 255–267. [CrossRef]
10. Li, C.; Deng, C.; Li, S.; Yuan, M.; Alam, M.; Liu, B.; Zhao, Z.; Li, W.; Yang, Y. Geochronology and genesis of the newly discovered Mengdehe orogenic-type Au deposit in the Xing'an-Mongolia orogenic Belt, NE China. *Ore Geol. Rev.* **2021**, *133*, 104083. [CrossRef]
11. Gao, S.; Xu, H.; Zang, Y.Q.; Wang, T. Mineralogy, ore-forming fluids and geochronology of the Shangmachang and Beidagou gold deposits, Heilongjiang province, NE China. *J. Geochem. Explor.* **2018**, *188*, 137–155. [CrossRef]
12. McNulty, B.A.; Jowitt, S.M. Byproduct critical metal supply and demand and implications for the energy transition: A case study of tellurium supply and CdTe PV demand. *Renew. Sustain. Energy Rev.* **2022**, *168*, 112838. [CrossRef]
13. Zweibel, K. The impact of Tellurium supply on Cadmium Telluride photovoltaics. *Science* **2010**, *328*, 699–701. [CrossRef] [PubMed]
14. Fornari, C.I.; Bentmann, H.; Morelhão, S.L.; Peixoto, T.R.F.; Rappl, P.H.O.; Tcakaev, A.; Zabolotnyy, V.; Kamp, M.; Lee, T.; Min, C.; et al. Incorporation of Europium in Bi_2Te_3 topological insulator epitaxial films. *J. Phys. Chem. C* **2020**, *124*, 16048–16057. [CrossRef]
15. Steven, B.; William, M.; Jinxue, W.; Michael, J.; Farzin, A. Advances in HgCdTe APDs and LADAR receivers. In Proceedings of the Infrared Technology and Applications XXXVI, Orlando, FL, USA, 5–9 April 2010; SPIE: Bellingham, WA, USA, 2010; Volume 7660.
16. Gu, H.J.; Li, B.W.; Li, C.L.; Yang, W.P.; Yang, Y.J.; Shi, H.L.; Zhang, M.M. The Discovery and Significance of Tellurideinthe Sanhetun Gold Deposit inthe Northeastern Great Xing'an Range. *Mineral. Petrol.* **2023**, *43*, 94–104, (In Chinese with English Abstract).
17. Liu, Y.; Li, W.; Feng, Z.; Wen, Q.; Neubauer, F.; Liang, C. A review of the Paleozoic tectonics in the eastern part of Central Asian Orogenic Belt. *Gondwana Res.* **2017**, *43*, 123–148. [CrossRef]
18. Zhang, B.; Xu, K.; Khan, U.; Li, X.; Du, L.; Xu, Z. A lightweight convolutional neural network with end-to-end learning for three-dimensional mineral prospectivity modeling: A case study of the Sanhetun Area, Heilongjiang Province, Northeastern China. *Ore Geol. Rev.* **2023**, *163*, 105788. [CrossRef]
19. Liu, B.S.; Kou, L.L.; Zhang, C.P.; Li, C.L.; Luo, J.; Han, R.P.; Li, B.W. Research on the relationship between mineralization and zircon LA-ICP-MS U-Pb dating of the mylonite from the Sanhetun gold deposit in Nenjiang region, Heilongjiang Province (in Chinese with English abstract). *Acta Geol. Sin.* **2022**, *96*, 954–970.
20. Zhou, J.; Wilde, S.A.; Zhao, G.; Han, J. Nature and assembly of microcontinental blocks within the Paleo-Asian Ocean. *Earth-Sci. Rev.* **2018**, *186*, 76–93. [CrossRef]
21. Miao, L.C.; Fan, W.M.; Zhang, F.Q.; Liu, D.Y.; Jian, P.; Shi, G.H.; Tao, H.; Shi, Y.R. Zircon SHRIMP geochronology of the Xinkailing-Keluo complex in the northwestern Lesser Xing'an Range, and its geological implications. *Chin. Sci. Bull.* **2003**, *48*, 2315–2323.

22. Li, B.W.; Gu, H.J.; Li, C.L.; Liu, B.S.; Yang, X.P. Geological Characteristics and Prospecting Potential of Sanhetun Gold Deposit in Heilongjiang Province. *Gold Sci. Technol.* **2022**, *30*, 508–517, (In Chinese with English Abstract).
23. Wang, F.Y.; Ge, C.; Ning, S.Y.; Nie, L.Q.; Zhong, G.X.; White, N.C. A new approach to LA-ICP-MS mapping and application in geology. *Acta Petrol. Sin.* **2017**, *33*, 3422–3436, (In Chinese with English Abstract).
24. Deditius, A.P.; Utsunomiya, S.; Reich, M.; Kesler, S.E.; Ewing, R.C.; Hough, R.; Walshe, J. Trace metal nanoparticles in pyrite. *Ore Geol. Rev.* **2011**, *42*, 32–46. [CrossRef]
25. Ciobanu, C.L.; Cook, N.J.; Utsunomiya, S.; Kogagwa, M.; Green, L.; Gilbert, S.; Wade, B. Gold-telluride nanoparticles revealed in arsenic-free pyrite. *Am. Miner.* **2012**, *97*, 1515–1518. [CrossRef]
26. Gregory, D.D.; Large, R.R.; Halpin, J.A.; Baturina, E.L.; Lyons, T.W.; Wu, S.; Danyushevsky, L.; Sack, P.J.; Chappaz, A.; Maslennikov, V.V.; et al. Trace Element Content of Sedimentary Pyrite in Black Shales. *Econ. Geol.* **2015**, *110*, 1389–1410. [CrossRef]
27. Zhang, J.; Deng, J.; Chen, H.; Yang, L.; Cooke, D.; Danyushevsky, L.; Gong, Q. LA-ICP-MS trace element analysis of pyrite from the Chang'an gold deposit, Sanjiang region, China: Implication for ore-forming process. *Gondwana Res.* **2014**, *26*, 557–575. [CrossRef]
28. Deditius, A.P.; Utsunomiya, S.; Ewing, R.C.; Kesler, S.E. Nanoscale "liquid" inclusions of As-Fe-S in arsenian pyrite. *Am. Miner.* **2009**, *94*, 391–394. [CrossRef]
29. Fleet, M.E.; Mumin, A.H. Gold-bearing arsenian pyrite and marcasite and arsenopyrite from Carlin Trend gold deposits and laboratory synthesis. *Am. Miner.* **1997**, *82*, 182–193. [CrossRef]
30. Keith, M.; Smith, D.J.; Jenkin, G.R.T.; Holwell, D.A.; Dye, M.D. A review of Te and Se systematics in hydrothermal pyrite from precious metal deposits; insights into ore-forming processes. *Ore Geol. Rev.* **2018**, *96*, 269–282. [CrossRef]
31. Deditius, A.P.; Utsunomiya, S.; Renock, D.; Ewing, R.C.; Ramana, C.V.; Becker, U.; Kesler, S.E. A proposed new type of arsenian pyrite: Composition, nanostructure and geological significance. *Geochim. Cosmochim. Acta* **2008**, *72*, 2919–2933. [CrossRef]
32. Qian, G.; Brugger, J.; Testemale, D.; Skinner, W.; Pring, A. Formation of As(II)-pyrite during experimental replacement of magnetite under hydrothermal conditions. *Geochim. Cosmochim. Acta* **2013**, *100*, 1–10. [CrossRef]
33. Deditius, A.P.; Reich, M.; Kesler, S.E.; Utsunomiya, S.; Chryssoulis, S.L.; Walshe, J.; Ewing, R.C. The coupled geochemistry of Au and As in pyrite from hydrothermal ore deposits. *Geochim. Cosmochim. Acta* **2014**, *140*, 644–670. [CrossRef]
34. Reich, M.; Kesler, S.E.; Utsunomiya, S.; Palenik, C.S.; Chryssoulis, S.L.; Ewing, R.C. Solubility of gold in arsenian pyrite. *Geochim. Cosmochim. Acta* **2005**, *69*, 2781–2796. [CrossRef]
35. Barker, S.L.L.; Hickey, K.A.; Cline, J.S.; Dipple, G.M.; Kilburn, M.R.; Vaughan, J.R.; Longo, A.A. Uncloaking invisible gold: Use of nanoSIMS to evaluate gold, trace elements, and sulfur isotopes in pyrite from Carlin-type gold deposits. *Econ. Geol.* **2009**, *104*, 897–904. [CrossRef]
36. Tanner, D.; Henley, R.W.; Mavrogenes, J.A.; Holden, P. Sulfur isotope and trace element systematics of zoned pyrite crystals from the El Indio Au–Cu–Ag deposit, Chile. *Contrib. Mineral. Petrol.* **2016**, *171*, 33. [CrossRef]
37. Du, B.; Shen, J.; Santosh, M.; Liu, H.; Liu, J.; Wang, Y.; Xu, K. Textural, compositional and isotopic characteristics of pyrite from the Zaozigou gold deposit in West Qinling, China: Implications for gold metallogeny. *Ore Geol. Rev.* **2021**, *130*, 103917. [CrossRef]
38. Li, C. Characteristics of Structural Superimposed Halo and Deep Prospecting Prediction of Yongxin Gold Deposit, Duobaoshan Area, Heilongjiang Province. *Geoscience* **2023**, *37*, 674–689, (In Chinese with English Abstract).
39. Ohmoto, H. Systematics of Sulfur and Carbon Isotopes in Hydrothermal Ore Deposits. *Econ. Geol.* **1972**, *67*, 551–578. [CrossRef]
40. Chaussidon, M.; Lorand, J. Sulphur isotope composition of orogenic spinel lherzolite massifs from Ariege (North-Eastern Pyrenees, France): An ion microprobe study. *Geochim. Cosmochim. Acta* **1990**, *54*, 2835–2846. [CrossRef]
41. Cooke, D.R.; McPhail, D.C. Epithermal Au-Ag-Te Mineralization, Acupan, Baguio District, Philippines: Numerical Simulations of Mineral Deposition. *Econ. Geol.* **2001**, *96*, 109–131.
42. Grundler, P.V.; Brugger, J.; Etschmann, B.E.; Helm, L.; Liu, W.; Spry, P.G.; Tian, Y.; Testemale, D.; Pring, A. Speciation of aqueous tellurium(IV) in hydrothermal solutions and vapors, and the role of oxidized tellurium species in Te transport and gold deposition. *Geochim. Cosmochim. Acta* **2013**, *120*, 298–325. [CrossRef]
43. Ciobanu, C.L.; Birch, W.D.; Cook, N.J.; Pring, A.; Grundler, P.V. Petrogenetic significance of Au–Bi–Te–S associations: The example of Maldon, Central Victorian gold province, Australia. *Lithos* **2010**, *116*, 1–17. [CrossRef]
44. Cook, N.J.; Ciobanu, C.L.; Wagner, T.; Stanley, C.J. Minerals of the system Bi–Te–Se–S related to the tetradymite archetype: Review of classification and compositional variation. *Can. Mineral.* **2007**, *45*, 665–708. [CrossRef]
45. Rye, R.O. A review of the stable-isotope geochemistry of sulfate minerals in selected igneous environments and related hydrothermal systems. *Chem. Geol.* **2005**, *215*, 5–36. [CrossRef]
46. Williams-Jones, A.E.; Bowell, R.J.; Migdisov, A.A. Gold in Solution. *Elements* **2009**, *5*, 281–287. [CrossRef]
47. Cook, N.J.; Ciobanu, C.L.; Mao, J.W. Textural control on gold distribution in As-free pyrite from the Dongping, Huangtuliang and Hougou gold deposits, North China Craton (Hebei Province, China). *Chem. Geol.* **2009**, *264*, 101–121. [CrossRef]
48. Möller, P.; Kersten, G. Electrochemical accumulation of visible gold on pyrite and arsenopyrite surfaces. *Miner. Depos.* **1994**, *29*, 404–413. [CrossRef]
49. Laird, J.S.; Halfpenny, A.; Ryan, C.G.; Liu, W. Evidence supporting micro-galvanic coupling in sulphides leads to gold deposition. *Contrib. Mineral. Petrol.* **2021**, *176*, 1–19. [CrossRef]
50. Peterson, E.C.; Mavrogenes, J.A. Linking high-grade gold mineralization to earthquake-induced fault-valve processes in the Porgera gold deposit, Papua New Guinea. *Geology* **2014**, *42*, 383–386. [CrossRef]

51. Douglas, N.; Mavrogenes, J.; Hack, A.; England, R. The liquid bismuth collector model: An alternative gold deposition mechanism. In *Understanding Planet Earth*; Skilbeck, C.G., Hubble, T.C.T., Eds.; Searching for a Sustainable Future; on the Starting Blocks of the Third Millennium: Australian Geological Convention, 15th, Sydney, Abstracts: Sydney; Geological Society of Australia: Sydney, Australia, 2000; 135p.
52. Tooth, B.; Brugger, J.; Ciobanu, C.; Liu, W. Modeling of gold scavenging by bismuth melts coexisting with hydrothermal fluids: An experimental study. *Geology* **2008**, *36*, 815–818. [CrossRef]
53. Tooth, B.; Ciobanu, C.L.; Green, L.; O Neill, B.; Brugger, J. Bi-melt formation and gold scavenging from hydrothermal fluids: An experimental study. *Geochim. Cosmochim. Acta* **2011**, *75*, 5423–5443. [CrossRef]
54. Jian, W.; Mao, J.W.; Lehmann, B.; Cook, N.J.; Xie, G.Q.; Liu, P.; Duan, C.; Alles, J.; Niu, Z.J. Au-Ag-Te-rich melt inclusions in hydrothermal gold-quartz veins, Xiaoqinling Lode Gold District, central China. *Econ. Geol.* **2021**, *116*, 1239–1248. [CrossRef]
55. Jian, W.; Mao, J.; Lehmann, B.; Cook, N.J.; Li, J.; Song, S.; Zhu, L. Hyper-enrichment of gold via quartz fracturing and growth of polymetallic melt droplets. *Geology* **2024**, *52*, 411–416. [CrossRef]
56. Frost, B.R.; Mavrogenes, J.A.; Tomkins, A.G. Partial melting of sulfide ore deposits during medium- and high-grade metamorphism. *Can. Mineral.* **2002**, *40*, 1–18. [CrossRef]
57. Cockerton, A.B.D.; Tomkins, A.G. Insights into the Liquid Bismuth Collector Model through Analysis of the Bi-Au Stormont Skarn Prospect, Northwest Tasmania. *Econ. Geol.* **2012**, *107*, 667–682. [CrossRef]
58. Oberthur, T.; Weiser, T.W. Gold-bismuth-telluride-sulphide assemblages at the Viceroy Mine, Harare-Bindura-Shamva greenstone belt, Zimbabwe. *Mineral. Mag.* **2008**, *72*, 953–970. [CrossRef]
59. Pals, D.W.; Spry, P.G. Telluride mineralogy of the low-sulfidation epithermal Emperor gold deposit, Vatukoula, Fiji. *Mineral. Petrol.* **2003**, *79*, 285–307. [CrossRef]
60. Bi, S.J.; Li, J.W.; Zhou, M.F.; Li, Z.K. Gold distribution in As-deficient pyrite and telluride mineralogy of the Yangzhaiyu gold deposit, Xiaoqinling district, southern North China craton. *Miner. Depos.* **2011**, *46*, 925–941. [CrossRef]